Mesoscale Transport of Enveloped Viruses

Daniela Moreno-Chaparro∗,[1,2] Florencio Balboa Usabiaga,[1] Marco Ellero,[1,3,4] and Nicolas Moreno †[1]
[1)] *Basque Center for Applied Mathematics, BCAM. Alameda de Mazarredo 14 , Bilbao 48400, Spain*
[2)] *University of the Basque Country/Euskal Herriko Unibertsitatea. Barrio Sarriena Leioa, 48940, Spain*
[3)] *Ikerbasque, Basque Foundation for Science, Calle de Maria Diaz de Haro 3, 48013, Bilbao, Spain*
[4)] *Complex Fluids Research Group, Department of Chemical Engineering, Faculty of Science and Engineering, Swansea University, Swansea SA1 8EN, United Kingdom*

(*Electronic mail: †nmoreno@bcamath.org)

(*Electronic mail: ∗ dmoreno@bcamath.org)

(Dated: 3 July 2025)

Enveloped viruses are characterized by spike proteins that protrude from and decorate the viral membrane. These proteins play a crucial role in host cell interactions and exhibit dynamic behaviors, such as tilting, sliding, and clustering, which vary across different types of enveloped viruses. For instance, SARS-CoV-2 spikes tilt to facilitate receptor binding, Influenza spikes migrate during infection, and HIV spikes migrate and cluster to enhance infectivity. In this study, we investigate how such dynamics influence the virus mobility. We characterize viral mobility through translational and rotational diffusion coefficients using a mesoscopic model that incorporates the dynamics of both the flexible spike proteins and the viral envelope. Using the smoothed dissipative particle dynamics (SDPD) method, we construct three virion models with varying spike flexibility. The first is a fully rigid virus with static spikes, the second is a model with spikes that tilt but remain fixed in position, and the third is a model allowing both tilting and sliding of spikes across the envelope. Our results show that spike flexibility primarily affects rotational diffusion, whereas the envelope dominates translational mobility of the virus. We also explore spike clustering driven purely by hydrodynamic interactions. We identify that hydrodynamic interactions alone can be responsible for dynamic clustering of spike proteins. Where, the characteristic size and lifespan of such clusters indicate predominantly doublets and triplets formations. Our findings highlight the role of spike dynamics in whole virion mobility, and motivate further investigations with time-resolved experimental evidence to fully characterize clustering behavior.

Keywords: Enveloped virus modeling, passive transport, rotational diffusion, translational diffusion, flexible spike proteins.

I. INTRODUCTION

Viruses propagation and transmission have a significant impact on global-public health, as evidenced by the recent SARS-CoV-2 pandemic. Besides SARS-CoV-2, other enveloped viruses, such as HIV, herpes, dengue, and influenza have persisted for decades, continuing to cause fatalities and reduce quality of life worldwide. Enveloped viruses are characterized by a lipid bilayer membrane that encapsulates their genetic material. This membrane is decorated with spike proteins that play a crucial role in the virus's ability to infect host cells. These spike proteins can bind to specific receptors on the cell surface, facilitating fusion and subsequent viral replication.[1]

Spike proteins can exhibit different dynamic behaviors that has been associated with the virus's ability to infect host cells and evade the immune system. Depending on the virus type and the specific interactions involved, spike proteins can tilt, diffuse, and cluster over the viral envelope. For example, in SARS-CoV-2, the spike proteins have been reported to exhibit a tilting motion (ranging from 25°–30°) that enhance their ability to bind to host cell receptors.[2,3] For Influenza viruses, the migration and localization of surface proteins has been identified as a hallmark during the infection process.[4–6] In the case of HIV, besides tilting[7] (ranging from 15°–25°) and diffusion of the surface proteins, recent studies suggested that the spike proteins can dynamically cluster, forming larger aggregates that can enhance the virus's infectivity.[7–11]

Understanding the dynamic behavior of viral spike proteins is critical for interpreting the mechanisms of viral entry. However, at the scale of the entire virion, the influence of spike protein dynamics on viral transport remains largely unexplored. These conformational and fluctuating motions can modulate both translational and rotational diffusion, thereby impacting the passive mobility of the virus through the fluid medium. Viral diffusion is a multiscale process governed by a complex interplay of factors, including virion size and geometry, medium viscosity, and hydrodynamic interactions with the environment. Importantly, thermally driven fluctuations in the spike proteins can alter mesoscale transport properties of the virion.

The coupling between microscopic spike protein dynamics and mesoscale virion mobility presents a fundamental challenge from both experimental and computational perspectives. Experimentally, a variety of advanced techniques

have been employed to probe the structural, mechanical, and functional properties of enveloped viruses.[8,12–18] While these tools have yielded valuable insights into virus assembly, deformation, and spike-mediated host interactions, they fall short of capturing the dynamic interplay between spike conformational changes and whole-virion transport. The simultaneous resolution of molecular fluctuations and mesoscale motion in fluid environments remains a formidable challenge.[19] On the computational front, numerical modeling has become indispensable in bridging these gaps.[20,21] Molecular dynamics (MD) simulations[22–25] offer atomistic-level resolution of viral structures and interactions, yet they are often limited by system size and timescale constraints. To overcome these limitations, a range of mesoscale modeling approaches has been developed, including Brownian dynamics,[26,27] coarse-grained (CG) models,[28,29] dissipative particle dynamics (DPD),[30–32] Monte Carlo simulations,[33] rigid bead-rod theory,[34,35] and rigid multi-blob (RMB) models.[36–38] While these methods enable the exploration of larger spatiotemporal scales and capture hydrodynamic effects, integrating fluctuating spike dynamics with realistic virion geometry and fluid-mediated interactions remains to be fully realized.

Recently, Moreno et al[37] adopted a rigid multi-blob model to characterize the translational and rotational diffusion of different enveloped viruses, exploring the effects of spike-proteins density and morphology. The viruses were modelled as fully-rigid objects, and their passive transport was associate solely on geometrical features. The authors postulated the existence of an optimal balance between viral rotational diffusion and interaction, modulated by the number of spike proteins.[37] The optimal condition showed to hold for the majority viruses investigated. However, viruses such as HIV, did not comply with this trend. This discrepancy suggested that the rigid models may not fully capture the effect of complex dynamics of HIV spike proteins[8–11] on the overall virion transport. This limitation of fully-rigid models motivates the development of more realistic virion models, where the translational degrees of freedom of the spike-proteins are relaxed.

Herein, we aim to develop a generalized mesoscopic model of spike/virion diffusion that bridges experimental and theoretical insights across spatial and temporal scales. To this end, we construct mesoscale models of enveloped virions suitable to study their diffusion, while accounting for spike-proteins dynamics. We model the hydrodynamic interactions between the virion and the surrounding fluid using the Smoothed Dissipative Particle Dynamics[39,40] (SDPD) method. We extend the rigid represention of the virions used by Moreno and coauthors,[37] by modelling the spike proteins and envelope as separate rigid bodies. This allow us to account for various spike proteins dynamics such as tilting and diffusion over the envelope. We analyze the change in the translational and rotational diffusion of the virions, with the variations in the spike proteins dynamics. Additionally, given the relevance of spike proteins clustering in viral infectivity,[8–11] we explore the applicability of our mesoscale virion models to capture clustering behavior of spike proteins, mainly dominated by hydrodynamic interactions.

In the remainder of this document, in Section II, we present the discretization and modeling of the virions. In Section III, we present the diffusional results for virions with different types of spike proteins dynamics, and discuss the implications of our finding in the transport properties of enveloped viruses. We finally explore the potential formation of spike proteins clusters mediated by hydrodynamic interactions.

II. METHODS AND MODELS

A. Smoothed Dissipative Particle Dynamics

SDPD is a mesoscale particle-based method widely used to model complex fluids, incorporating consistent thermal fluctuations of the dissipative particle dynamics[39,40] method and the discretization scheme of smoothed particle hydrodynamics.[41] SDPD has been successfully applied to model a wide range of complex systems, including synthetic[37,42] and biological[43,44] polymeric materials, multiphase flows,[45] colloids,[46] and red blood cells to name a few. In this framework, we discretize both the virus and the surrounding fluid into small spherical particles. The SDPD method incorporates both conservative and dissipative forces, as well as random thermal fluctuations, to model the interactions between particles. Each particle is characterized by its position $\mathbf{r}_i$, velocity $\mathbf{v}_i$, mass m_i, and a volume V_i, such that $1/V_i = d_i = \sum_j W(r_{ij},h)$. Here d_i is the number density of particles, $r_{ij} = |\mathbf{r}_i - \mathbf{r}_j|$, and $W(r_{ij},h)$ is an interpolant kernel with finite support h. In 3D, we use the kernel $W(r) = 105/(16\pi h)(1+3r/h)(1-r/h)^3$ if $r/h < 1$ or $W(r) = 0$ if $r/h \geq 1$.[39]

The evolution equations for the particles position is $\mathrm{d}\mathbf{r}_i/\mathrm{d}t = \mathbf{v}_i$, whereas the momentum equation takes the form

$$\begin{aligned} m_i \frac{\mathrm{d}\mathbf{v}_i}{\mathrm{d}t} = & \underbrace{\sum_j \left[\frac{p_i}{d_i^2} + \frac{p_j}{d_j^2}\right] F_{ij}\mathbf{r}_{ij}}_{\text{conservative}} \\ & - \underbrace{\sum_j \left[a\mathbf{v}_{ij} + b(\mathbf{v}_{ij}\cdot\mathbf{e}_{ij})\mathbf{e}_{ij}\right] \frac{F_{ij}}{d_i d_j}}_{\text{dissipative}} \\ & + \underbrace{\sum_j \left(A_{ij}\mathrm{d}\overline{\mathbf{W}}_{ij} + B_{ij}\frac{1}{3}\mathrm{tr}[\mathrm{d}\mathbf{W}_{ij}]\right)\cdot\frac{\mathbf{e}_{ij}}{\mathrm{d}t}}_{\text{random}}, \end{aligned} \tag{1}$$

where $\mathbf{e}_{ij} = \mathbf{r}_{ij}/|\mathbf{r}_{ij}|$, $\mathbf{v}_{ij} = \mathbf{v}_i - \mathbf{v}_j$, a and b are friction coefficients related to the shear η and bulk ζ viscosities of the fluid through $a = 5\eta/3 - \zeta$ and $b = 5(\zeta + \eta/3)$. In Eq. 1, we introduce the positive function $F_{ij} = -\nabla W(r_{ij},h)/r_{ij}$. The term

$\overline{\mathbf{W}}_{ij}$ is a matrix of independent increments of a Wiener process for each pair i, j of particles, and $\overline{\mathbf{W}}_{ij}$ is its traceless symmetric part, given by $\mathrm{d}\overline{\mathbf{W}}_{ij} = 1/2\left[d\mathbf{W}_{ij} + \mathrm{d}\mathbf{W}_{ij}^T\right] - \delta^{\alpha\beta}/3\mathrm{tr}[\mathrm{d}\mathbf{W}_{ij}]$. To satisfy the fluctuation-dissipation balance the amplitude of the thermal noises A_{ij} and B_{ij} are related to the friction coefficients a and b through $A_{ij} = [4k_BTaF_{ij}/\rho_i\rho_j]^{1/2}$ and $B_{ij} = [4k_BT(b-a/3)F_{ij}/\rho_i\rho_j]^{1/2}$, where k_BT is the thermal energy, and ρ_i and ρ_j are the densities of the particles i and j. The pressure p_i of the i-th particle is estimated using an equation of state of the form $p_i = c^2\rho_0/7[(\rho_i/\rho_0)^7 - 1]$, where c is the artificial speed of sound on the fluid, and ρ_0 is the reference density. The term $c^2\rho_0/7$ sets the speed of sound at the reference pressure, $c^2 = \partial p/\partial\rho|_{\rho=\rho_0}$.

B. Mesoscale Virion Models

We construct three mesoscale virion models to investigate the effect of spike proteins dynamics over the passive transport of enveloped viruses. These models corresponds to a spherical envelope decorated with (1) rigidly connected spikes proteins, (2) fixed-position pivoting spikes proteins, and (3) freely-sliding/pivoting spikes proteins, as illustrated in FIG. 1a.

1. Model 1

In Model 1, the whole virion (envelope and spike proteins) is represented as a rigid body, where the spike proteins are uniformly distributed over the surface of the envelope. This initial approximation serves as a reference point for comparing the effects of spike flexibility in subsequent models, and allows us to compare with the prior diffusional studies by Moreno et al,[37] where the surrounding fluid was modeled implicitly using the Rigid Multi-Blob (RMB) method.

2. Model 2

In Model 2, we assess how spike tilting affects the whole-virion diffusion. Here, spike proteins are represented as independent rigid bodies and are allowed to pivot at fixed positions over the envelope. Two additional potentials govern spike-envelope interactions. First, the spike protein is anchored to a fixed position over the envelope surface (as occur in model 1), *via* an harmonic spring potential, $E = (1/2)K(x_{se} - x_0)^2$, where K is the spring constant, $x_{se} = |\mathbf{p}_1 - \mathbf{p}_2|$ the distance between two prescribed particles in the spike protein and the envelope respectively, and $x_0 = dx$ is the equilibrium distance of the potential, defined to be near the equilibrium SDPD interparticle distance (dx), to prevent artificial density variations.

MD studies often describe spike proteins tilting using multi-joint structure[2] (hip-knee-foot) with cumulative articulation angles. Here, we adopt a single pivot located at the base of each spike proteins describing an effective tilting angle with respect to the envelope's surface, *via* an harmonic angular spring potential. This potential is given by $E_\alpha = (1/2)K_\alpha(\theta - \theta_0)^2$, where K_α is a constant that controls the stiffness, θ_0 is the equilibrium angle, and θ is the angle formed between a fixed point in the envelope surface ($\mathbf{p}_1$), a point in the protein base ($\mathbf{p}_2$), and the protein tip ($\mathbf{p}_3$), as illustrated in Fig. 1.c.1.

In our virions, we define the tilting angle $\beta = |\theta - \theta_0|$ of the spike proteins to prescribe a favored orientation, and K_α tunes the degree of flexibility of the protein with respect to this orientation. Here, we set an equilibrium angle $\theta_0 = 180^o$, corresponding to a perpendicular alignment over the envelope surface. In the limit $K_\alpha \to \infty$, the spike protein remains perpendicular to the surface fixed point, $\beta \to 0$. Whereas, as $K_\alpha < \infty$, we expect $\beta > 0$ as the thermal fluctuations become relevant. In the results section, we show that the magnitude of β can be effectively adjusted by varying K_α. Additionally, we compare with the theoretical expectation derived from the probability distribution of the intrinsic tilting angle β. Given the angular potential adopted, the distribution function reads $P(\beta) = Z^{-1}\sin(\beta)\exp\left(-K_\alpha(\beta)^2/2k_BT\right)$, where Z is a normalization constant that ensures the integral of the probability function is equal to one, $\int_0^\pi P(\beta)d\beta = 1$. This expression enables estimation of the expected values of β as a function of K_α, providing a theoretical baseline for comparison with our simulation results.

3. Model 3

In Model 3, the spike proteins can both pivot and slide over the envelope surface. This configuration introduces additional degrees of freedom associated with the free diffusion of spike proteins over the envelope's surface. Similar to Model 2, we use two harmonic potentials to constraint the position and tilting. In this case, the spike proteins are anchored to the envelope center of mass, $\mathbf{p}_1$, with an harmonic potential at an equilibrium distance $x_0 = R + dx$, as illustrated in FIG. 1.c.2. The control over the tilting angle is modeled using an harmonic angular potential, where the angle θ is formed between the envelope's center of mass $\mathbf{p}_1$, a point in the protein base ($\mathbf{p}_2$), and the protein tip ($\mathbf{p}_3$), as shown in FIG. 1.c.2. The equilibrium angle is $\theta_0 = 180^o$, ensuring an alignment of the spike protein normal to the envelope's center of mass. For model 3, the hydrodynamic interactions with the surrounding fluid can induce both translation and tilting of the spike proteins. Since we are not explicitly accounting for translational constraints (besides fluid drag), we vary the surface protein stiffness to investigate scenarios where either sliding or tilting dynamics can be dominant.

Moreover, we explore a variant of Model 3 where the spike proteins move over a fixed envelope to simulate membrane-bound behavior. Thus, we also compute the geodesic mean-squared displacement (gMSD) of the spike proteins (see Appendix H for detailed description) to estimate their effective translational diffusion D_{sp} over the envelope. In principle, since D_{sp} can be affected by the amount of

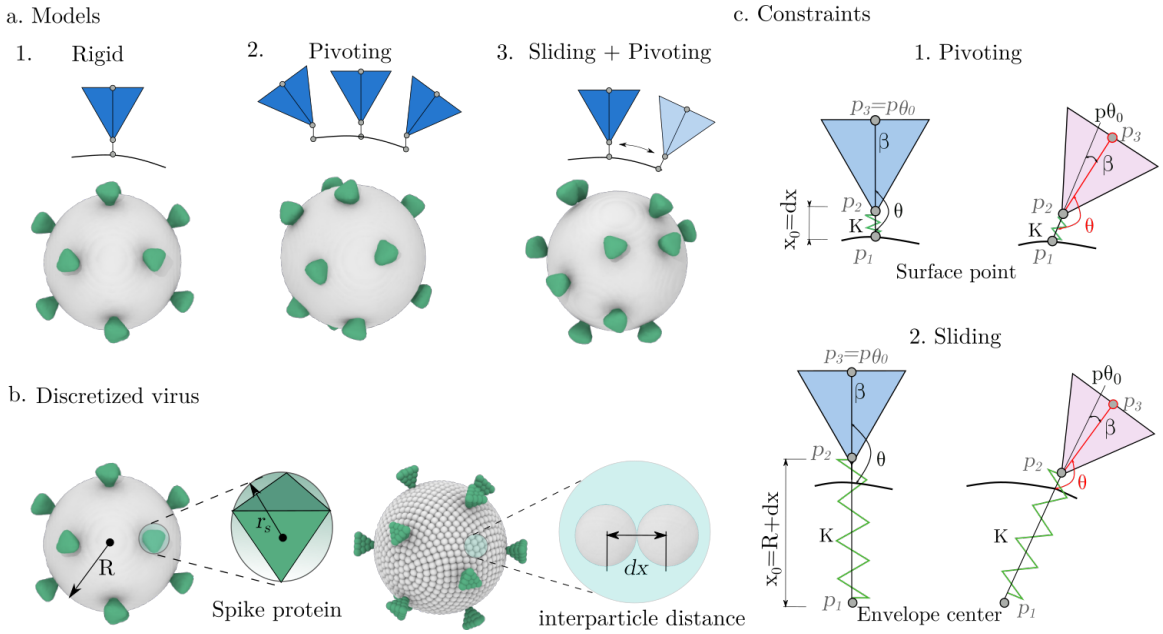

FIG. 1. (a.)Schematic representation of the three virus models. spikes proteins are modeled as tetrahedral structures and are uniformly distributed over a spherical envelope. Model 1 features rigid spikes proteins, model 2 allows pivoting (tilting) motion, and model 3 incorporates both pivoting and sliding (free diffusion). (b) Discretization of a virion with envelope radius R and tetrahedral spike-protein radius r_s, in SDPD. dx denotes the interparticle distance. (c.) Linear harmonic potential constraint, here, spring constant K, anchors each spike-protein base to the envelope. The distance x_{se} is measured between the points $|\mathbf{p}_1 - \mathbf{p}_2|$. The spring equilibrium distance is $x_0 = dx$ for the pivoting case (c.1) and $x_0 = R + dx$ for the sliding case (c.2). For the angular harmonic potential constraint, the spring constant K_α controls the stiffness in three points $\mathbf{p}_1, \mathbf{p}_2, \mathbf{p}_3$. Here, we define θ as the angle formed between these three points, with an equilibrium angle $\theta_0 = 180$. Blue spike protein illustrate $\theta = \theta_0$, when $\mathbf{p}_3 = \mathbf{p}\theta_0$. Tilting angle $\beta > 0$ amounts for deviations from the equilibrium case (pink spike proteins).

decorating proteins, we vary the numbers N_{sp} of spike proteins, ranging from 2-24 per envelope, to investigate the presence of a crowding effect.

C. Whole-Virion Passive Transport

To analyze the impact of spike-protein dynamics on virus mobility, we compute the translational (D_t) and rotational (D_r) diffusion coefficients using the mean square displacement (MSD $= 6D_t t$) and mean square angular displacement (MSAD $= 4D_r t$) (See Appendix F-G), respectively.[46–48] For the each of the models evaluated, we perform three independent realizations to ensure statistical robustness. D_t and D_r are estimated from the MSD in the range $10\tau_\nu$ to $100\tau_\nu$, where $\tau_\nu = \rho R^2/\eta$ is the kinematic time, ρ is the density mass, R is the envelope radius and η the viscosity.

While factors such as size, shape, number, and distribution of spike proteins influence virion transport,[37] this study focuses solely on the effects of spike dynamics. For generality, we model enveloped virions with a spike-to-envelope size ratio of $r_s/R = 2/10$, where r_s is the spike radius. Inspired by HIV and SARS-CoV-2 structures, we represent spikes proteins as tetrahedral-like shapes, with r_s defined as the radius of the sphere inscribing the tetrahedron. Unless otherwise stated, we use a fixed number of twelve uniformly distributed spikes proteins (see FIG. 1.b), consistent with experimental observations of HIV virions.[37]

D. Spike-proteins Clustering

We investigate the occurrence of dynamic spike-proteins clustering mediated by hydrodynamic interactions in model type 3, where the spike proteins can freely diffuse over the envelope. When any particle belonging to one spike protein is within a clustering cutoff radius $r_{cl} = 5dx$, of a particle from another spike protein, we consider the spike proteins form part of the same cluster. To monitor the temporal evolution of cluster formation throughout the simulation, we perform a clustering analysis on simulation snapshots taken every $1000\Delta t$. The total number N of clusters and number C_s of spike proteins per cluster is measured to estimate the *lifetime* $l_t(C_s)$. The lifetime $l_t(C_S)$ is the cumulative time (not necessarily consecutively) that clusters of size i are observed during the simulations. We rationalize the relevance of the times scales of spike-proteins clustering events, with respect to the characteristic diffusive time $\tau_{\text{sat}} = R^2/D_{sp}$ of the spike proteins over the envelope surface. Thus we define the normalized lifetime

$$l_t(C_s) = \frac{1000\Delta t S_i}{N_i \tau_{\text{sat}}}, \tag{2}$$

where S_i is the total number of snapshots that a cluster with size $C_s = i$ appear in the simulation, and N_i is the number of

such clusters. We also define the *lifespan* $\Delta s(i)$ as the number of consecutive snapshots during which cluster of size C_s remains. Further reappearances are treated as new lifespan event. Thus, the mean lifespan is given by

$$\langle \Delta s(i) \rangle = \frac{1000\Delta t}{\tau_{\text{sat}} M_i} \sum_{n=1}^{M_i} \Delta s(i)_n \tag{3}$$

where M_i is the total number of lifespan events observed during the simulation for a cluster of size $C_s = i$.

E. Simulation Setup and Parameters

As is customary in SDPD simulations, we adopt a system of dimensionless (reduced) units by defining characteristic scales for length (l_{sdpd}), mass (m_{sdpd}), and energy ($\varepsilon_{\text{sdpd}}$). Consequently the characteristic time unit is $\tau_{\text{sdpd}} = l_{\text{sdpd}}(m_{\text{sdpd}}/\varepsilon_{\text{sdpd}})^{1/2}$. All quantities are expressed in terms of these fundamental units. In all the simulations, we use periodic cubic domains with size $L_b = 15 l_{\text{sdpd}}$. The interparticle distance is set to $dx = 0.2[l_{\text{sdpd}}]$, leading to an equilibrium particle density $d = 1/dx^3[l_{\text{sdpd}}^{-3}]$, whereas the size of the interpolation kernel is $h = 4dx$, ensuring that hydrodynamic interactions are accurately captured while maintaining computational efficiency.[49]

In our discretization, the envelope and spike proteins are formed by SDPD particles located with an interparticle distance $dx = (1/d)^{1/3}$, where d is the particle number density of the simulation. We define the resolution of the virion model from the ratio R/dx, where R is the radius of the envelope. To determine an appropriate resolution, we conduct a convergence study (see Appendix A-B) examining the rotational mobility of spherical envelopes. We find that a resolution of $R/dx = 10$ offers an optimal trade-off between computational efficiency and consistency with theoretical predictions from Stokes-Einstein theory.[50] This choice ensures that the envelope is sufficiently resolved to capture both its translational and rotational dynamics while maintaining tractable computational cost for simulations involving the spike proteins. At this resolution, we quantify the numerical deviations of the simulated envelope diffusion coefficients (D_t^e and D_r^e) relative to theoretical Stokes–Einstein values: approximately 6% for translational and 24% for rotational diffusion. The larger deviation in the rotational component is attributed to its R^3 dependence, which enhances sensitivity to finite-size effects. However, considering that these numerical deviations are systematic and persist across all virion models considered, we follow the approach of Moreno et al,[37] introducing reduced diffusion coefficients

$$\bar{D}_n = \frac{D_n}{D_n^e}, \tag{4}$$

where D_n is the measured diffusion coefficient of a virion model (including spikes proteins), D_n^e is the corresponding value measured for the bare spherical envelope (without spikes proteins), and $n = t, r$ denotes the translational or rotational component, respectively. Eq.(4) allows us to normalize out numerical deviations and enable direct comparison between models. In the results section, we show that for the virion resolution adopted, we reproduce the rotational diffusion $\bar{D}_n$ previously reported for fully rigid models.[37]

For virion models with mobile spike proteins, we set the spring constant $K = 1000[\varepsilon_{\text{sdpd}}/l_{\text{sdpd}}^2]$, whereas different angular spring constant are explored $K_\alpha = \{8, 10, 100, 1000\}[\varepsilon_{\text{sdpd}}]$.

III. RESULTS AND DISCUSSION

A. Model 1: Fully-Rigid Model Diffusion

In FIG. 2a, we compile the MSD and MSAD curves (averaged over three realizations) for fully-rigid models. The linear variation of MSD consistently indicates a normal diffusion behavior of the virion. Similarly, MSAD exhibits normal diffusion at short times, but eventually saturates near the expected theoretical[48] bound $(\pi^2 - 4)/2$ due to angular confinement. In FIG. 2, the shaded green ($10\tau_v$ to $100\tau_v$) region highlight the intervals used to compute $\bar{D}_t$ and $\bar{D}_r$. The normalized diffusion coefficients obtained, $\bar{D}_t = 0.870 \pm 0.114$ and $\bar{D}_r = 0.673 \pm 0.009$, evidence a reduction in both translational and rotational diffusivity compared to the bare envelope. Remarkably, this results are in close agreement with the measured diffusion using RMB[38] with 12 uniformly distributed spike proteins ($\bar{D}_t = 0.87$ and $\bar{D}_r = 0.64$). These results support the accuracy of our SDPD implementation and the chosen resolution of the virion models.

B. Model 2: Pivoting Model Diffusion

We now examine the diffusion behavior of the virion models featuring flexible pivoting spike proteins. In FIG. 2.b, we present the MSD and MSAD curves averaged over three independent simulations for virions with tilting dynamics, with a mean tilting angle $\beta \approx 20^\circ$. Both curves exhibit a similar trend as the rigid model, with MSD showing linear growth and MSAD saturating near the theoretical limit $(\pi^2 - 4)/2$. The computed normalized diffusion coefficients for this model are $\bar{D}_t = 0.905 \pm 0.0184$ and $\bar{D}_r = 0.697 \pm 0.06$. Compared to the rigid virion model, the pivoting configuration has a slightly larger translational and rotational diffusion. This indicates that the tilting dynamics of the spike proteins do not hinder significantly virus mobility.

C. Model 3: Sliding and Pivoting

In FIG. 2.c, we compile the MSD and MSAD curves for the sliding model, varying the stiffness constant on the range $K_\alpha = \{10, 100, 1000\}[\varepsilon_{\text{sdpd}}]$ (see also Appendix D, Table III)for the summarized values of $\bar{D}_t$ and $\bar{D}_r$). In the

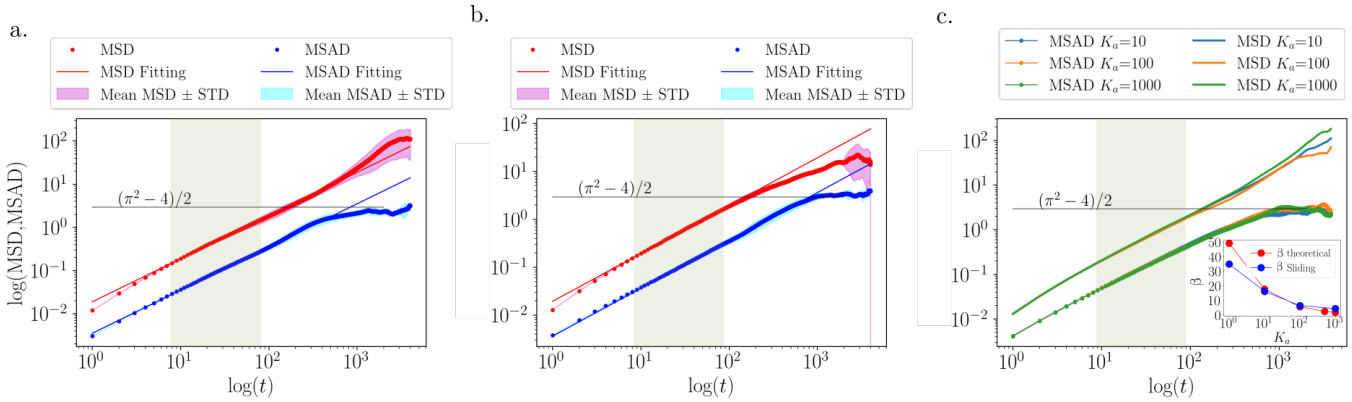

FIG. 2. a. MSD and MSAD log-log curves for the rigid virion models averaged over three independent realizations. The shaded green region marks the interval used to compute rotational diffusion $\bar{D}_r$, and translational diffusion $\bar{D}_t$. The MSAD curve saturates near the theoretical limit $(\pi^2-4)/2$. b. MSD and MSAD log-log curves for pivoting model and c. MSD and MSAD log-log curves for sliding models respectively for three different cases of K_α. We use the continuous lines for the MSD and the continues with dots for the MSAD. Inside plot, show the tilting angle β as a function of angular stiffness K_α (1 to 1000) for both theoretical predictions and simulation results on curved (envelope) surfaces. β is defined between three points: envelope center of mass (p_1), spike base (p_2), and spike tip (p_3). Higher K_α values restrict spike motion, reducing β. For the most flexible case, $K_\alpha = 1$, the theoretical and simulated angles differ because, in the simulation, the tetrahedral spike can collide with the envelope, diminishing the effective angle inclination.

inside plot of FIG. 2.c, we also show the dependency of the measured tilting angle β with K_α, to illustrate versatility of the model to reproduce a range of tilting angles. Consistent with theoretical predictions, increasing K_α reduces β, with angles approaching 0° at the highest stiffness evaluated ($K_\alpha = 1000\varepsilon_{\text{sdpd}}$). Conversely, at the lowest $K_\alpha = 1\varepsilon_{\text{sdpd}}$, the tilting angle can reach a mean angle 50°, indicating nearly unconstrained tilting.

In FIG. 2.c, we can observe that the translational diffusion remains relatively stable across different K_α values, with $\bar{D}_t \propto 1.0$, suggesting modest alterations with respect to the bare envelope, with variations falling within the range of simulation uncertainty. The slightly higher translational diffusion compared to the previous models, suggests that the spike proteins mobility may induce marginal gains in the translational motion, due to dynamic redistribution of hydrodynamic stresses. Regarding the rotational diffusion, virions with more flexible spike proteins (lower K_α) exhibit a slightly larger rotational mobility. This is consistent with previous observations in pivoting models, where the flexibility appears to reduce rotational drag.

D. Summary of Different Models and Implications

In FIG. 3, we summarize the variation of the translational and rotational diffusion for the free envelope and the different virion models investigated. We can identify that the dynamics of spike proteins over the envelope, are responsible for variations in $\bar{D}_t$, characterized by reductions around 10% for models with immobile spike proteins (model 1 and 2, rigid and pivoting, respectively). In contrast, virion model 3, with freely sliding spike proteins, exhibit a $\bar{D}_t \propto 1$ on the order of the free envelope. Moreover, FIG. 3.a shows that the tilting degree of the proteins induce only marginal variations in the translational diffusion of the virions, as evidence on the weak dependence of $\bar{D}_t$ with K_α.

In general, the impact of spike protein flexibility is small for the translational diffusion. However, for rotational diffusion spike proteins dynamics becomes more relevant. In FIG. 3.b, we can observe that both tilting and diffusion of the spike proteins alter the overall rotational motion of the virions. When comparing Models 1 (fully rigid) and 2 (immobile but freely tilting proteins), where spike proteins have a fixed position over envelope, the spike-protein tilting dynamics only induce a marginal increase in the rotational diffusion. In contrast, Model 3, where spike proteins can slide, exhibits the largest $\bar{D}_r$. This suggest that the sliding of the spike proteins can facilitate the dynamic redistribution of hydrodynamic stresses leading to an overall reduction in the rotational drag. Additionally, as the spike protein becomes more flexible (i.e. decreasing K_α), the marginal gains due to tilting dynamics, lead to $\bar{D}_r$ values converging to the bare envelope, indicating that envelope and spike-proteins mobility are decoupled.

Stemming from our current findings, we explore now the implications of $\bar{D}_r$ variations on the *excess diffusion* proposed by Moreno and coauthors.[37] The authors defined an excess rotational diffusion ΔD_r, given by $\Delta D_r = (\bar{D}_r - \bar{D}_r^\infty)/(1-\bar{D}_r^\infty)$, where $\bar{D}_r$ is the measured virion's rotational diffusion with a fixed number of spike proteins, and $\bar{D}_i^\infty$ is the asymptotic value in diffusion coefficient, as the number of spike proteins reaches N_s^∞, that is the saturation number of spikes. Thus, further addition of spike proteins over the envelope does not affect their mobility. Moreno and coauthors, postulate that for a given virion (e.g. HIV, SARS-CoV-2, Influenza), the variations in the excess diffusion can be expressed in terms of the

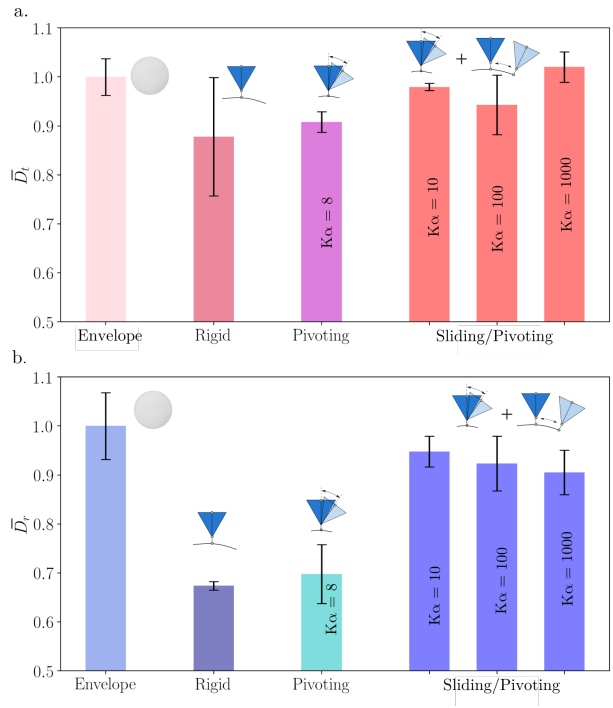

FIG. 3. Normalized translational ($\bar{D}_t$)(a.) and rotational ($\bar{D}_r$) (b.) diffusion coefficients for the three virus models: rigid, pivoting, and sliding. For the rigid model, $K_\alpha \to \infty$; for the pivoting model, $K_\alpha \approx 8$; and for the sliding model, K_α takes values of 10, 100, and 1000. First bar in both graphics indicate the baseline envelope diffusion coefficients for translation and rotation, respectively.

total number of spike proteins, $\Delta D_i = f(N_s)$, as

$$\Delta D_i = \frac{N_s^\infty - N_s}{N_s^\infty}[1 - e^{\frac{-b}{N_s}}], \tag{5}$$

where N_s^∞ is in general defined by the aspect ratio between the spike protein and the envelope, and b indicates the rate of decay in the rotational mobility. In Eq.(5), b is a fitting parameter characteristic for each type virus, and lower values indicate a faster decay of ΔD_i.

Models 2 and 3 can be associated with HIV virions with different state of maturation, where Model 2 corresponds to immature states, where the spike proteins are linked to the membrane and cannot diffuse[9,51–53]. Whereas Model 3 are consistent with mature states, when the capsid of the virus is already form and the spike proteins can translate along the membrane. We evaluate Eq. (5) for the three virion models, using a saturation value of $N_s^\infty = 146$ consistent for HIV.[37] We estimate the decay parameters to be $b_1 = 5.8$, $b_2 = 6.7$, and $b_3 = 25.7$, where the subindex denotes the model type. In FIG 4, we present ΔD_r as a function of N_s, and indicate the corresponding excess diffusion at $N_s = 12$. This number falls within the experimentally reported range for HIV, typically between 11 and 14. At such low spike densities, we observe that the transition from a mature to an immature state can significantly impact the rotational motion of the virion. This raises the question of whether the maturation state itself could serve as a regulatory feature to modulate transport properties. It is important to note that friction between the spike proteins and the membrane can influence their mobility, thereby affecting the overall diffusion of the virion. In our framework, Model 2 and Model 3 represent the limiting cases of spike diffusion—fully mobile and fully immobile spikes, respectively—with real systems likely exhibiting behavior somewhere between these extremes. For virions with a larger number of spike proteins, such as herpes virus, or for larger virions in general, the differences between these two models may become negligible, as the influence of individual spike mobility on overall transport diminishes.

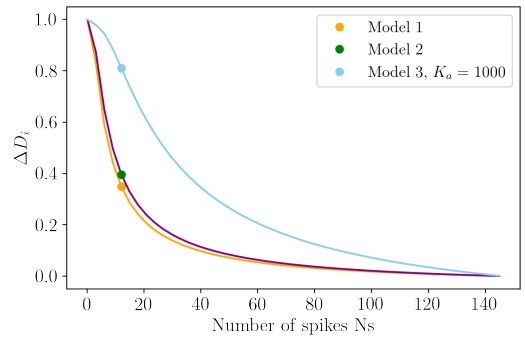

FIG. 4. Comparison rotational diffusion (ΔD_r) as a function of spike number (N_s) for flexible and rigid virus model. The solid orange curve represents the rigid virus model, while the purple and blue curves shows our flexible models. Here for model 2 and 3, b values are 6.7 and 25.7 respectively. Markers on all curves indicate values for 12 spikes proteins. A clear increase the HIV sliding model 3, highlighting the impact of spike flexibility on rotational diffusion.

E. Spike-Proteins Clustering Dynamics

Besides the effects of spike-protein dynamics on the whole-virion transport, we now use the mesoscale virion models to investigate the clustering dynamics of the spike proteins .

In FIG. 5, we compare the gMSD of the spike proteins over envelopes containing $N_s = 2, 12, 24$ proteins. In FIG. 5.a, we observe that the gMSD curves exhibit linear dependency at short times and saturate at long times $t > t_{\text{sat}} = R^2/D_{sp}$. The simulated virions show an equivalent behavior at short times and consistently saturate to values close to $R^2(\pi - 4)/2$.[48] From the gMSDs, we identify that the D_{sp} estimated (and consequently τ_{sat}) at short times show a weak dependency with the number of spike proteins simulated, indicating a diluted condition of spike proteins decorating the envelope (see Appendix I, Table IV). Thus, when estimating the lifetime of clusters in Eq. (2), we consider a fixed diffusional time $\tau_{\text{sat}} = 90\tau_{\text{sdpd}}$ regardless of the spike proteins density of the virion. We must highlight, that even though the measured

D_{sp} seems unaffected by the presence of other proteins, the hydrodynamic interactions between spike proteins are effectively influencing the proteins mobility. The plot in FIG. 5.b, shows the probability-density functions (PDFs) — estimated via kernel density estimation (KDE) — of the protein's squared-displacement ($\Delta\mathbf{x}^2$), at three different times (0.1, 10, 90 τ_{sdpd}). At shorter times, when spike proteins do not interact with others, the distributions remain the same for the different virions. For later times, the number of encounters should be favored for virions with more spike proteins, leading to the small variations observed in the displacements distribution. However, those variations do not affect the D_{sp} measured (for the number of spike proteins evaluated), as their influence is hindered by the saturation time scale of the gMSD. For virions with a larger number of spike proteins (i.e. Influenza virus[54] with $N_s > 400$), stronger variations in the displacements distribution would be expected (crowding effects), significantly altering the proteins transport at short time scales, and therefore the effective proteins diffusion D_{sp}.

In FIG. 6, we now summarize the clustering analysis of spike proteins mediated by hydrodynamic interactions, where we track the number of clusters N, cluster size C_s, lifetime $l_t(C_s)$ and lifespan $\Delta s(C_S)$. In FIG. 6.a, we evidence the existence of such clusters, and compare the histogram of N for virions with 12 and 24 spike proteins. We observe that virions with 12 spike proteins exhibit N values ranging from 5 to 12 clusters, with a mean $N \sim 9.5$. For 24 spike-proteins case, N ranges from 7 to 22, with a mean value $N \sim 15$. Note that isolated spike proteins are also accounted as clusters of size 1. Thus, in FIG. 6.b, we present the normalized frequencies of the cluster size C_s, omitting $C_s = 1$ to highlight the actual existence of spike proteins aggregates. For both virions, the largest frequencies measured correspond to $C_s = 2$ and $C_s = 3$. Even though larger clusters ($C_s > 3$) are also detected, they are significantly less likely for the number of spike-proteins investigated.

In FIG. 6.b, we further analyze the potential relevance of the formed protein clusters in terms of their *lifetime* Eq.(2) and *lifespan* Eq.(3). Consistent with the cluster size distributions, clusters of size $C_s = 2-3$ amount for largest lifetimes, with few larger clusters ($C_s = 4-5$) exhibiting noticeable lifetimes. However, when analyzing their lifespan, we observe that for cluster size $C_s > 3$ are less stable and tend to disperse quickly. Interestingly, although clusters of size $C_s = 3$ exhibit a short measured lifespan, their relatively high frequency suggests that they form frequently despite not persisting over time. Similar clusters containing three proteins have also been reported in the context of HIV,[51–53] raising the question of whether such recurring formations might serve a functional role. However, experimentally determining the lifespan of these clusters remains challenging, making it difficult to assess whether their duration is sufficient to facilitate viral entry. If a longer lifespan is indeed required for functionality, this would suggest that hydrodynamic interactions alone are insufficient to explain their formation. In that case, additional interactions—either between spike proteins themselves or between the proteins and the membrane—may be necessary. Although our model does not explicitly include attractive or repulsive interactions to promote clustering, our results demonstrate that hydrodynamic interactions alone can mediate the formation of spike protein clusters.

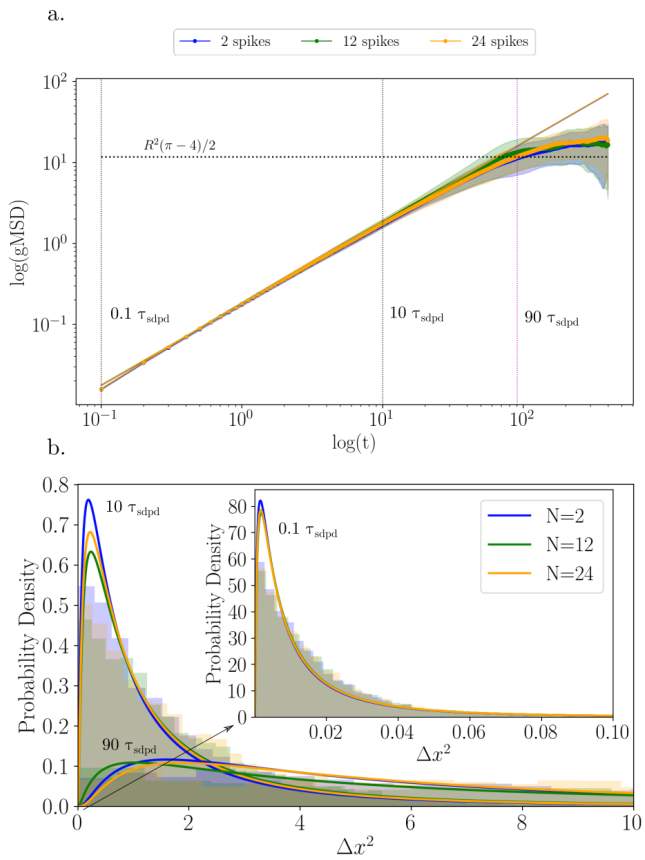

FIG. 5. a) gMSD log-log curves for spike protein diffusion on the viral envelope, comparing systems with 2, 12, and 24 spikes proteins. All configurations show similar diffusion dynamics, converging to a plateau due to spatial confinement. The dotted lines indicate three-time points: $0.1\tau_{\text{sdpd}}$, $10\tau_{\text{sdpd}}$, and $90\tau_{\text{sdpd}}$. b) Probability density functions (PDFs) of geodesic distances at $\Delta t = 0.1$, 10, and $90\tau_{\text{sdpd}}$ for systems with 2, 12, and 24 spikes proteins. KDE curves are computed from the average of three replicas (two for the 24-spike case).

IV. CONCLUSIONS

In this work, we investigated how spike flexibility influences the passive transport of viruses. Adopting mesoscale rigid-body descriptions, that incorporate spike flexibility features, together with a fluctuating hydrodynamics via the SDPD method, allows us to model more realistic virion dynamics on temporal and spatial scale of the whole virion. Additionally it offers an improved representation to investigate and understand viral transport and entry.

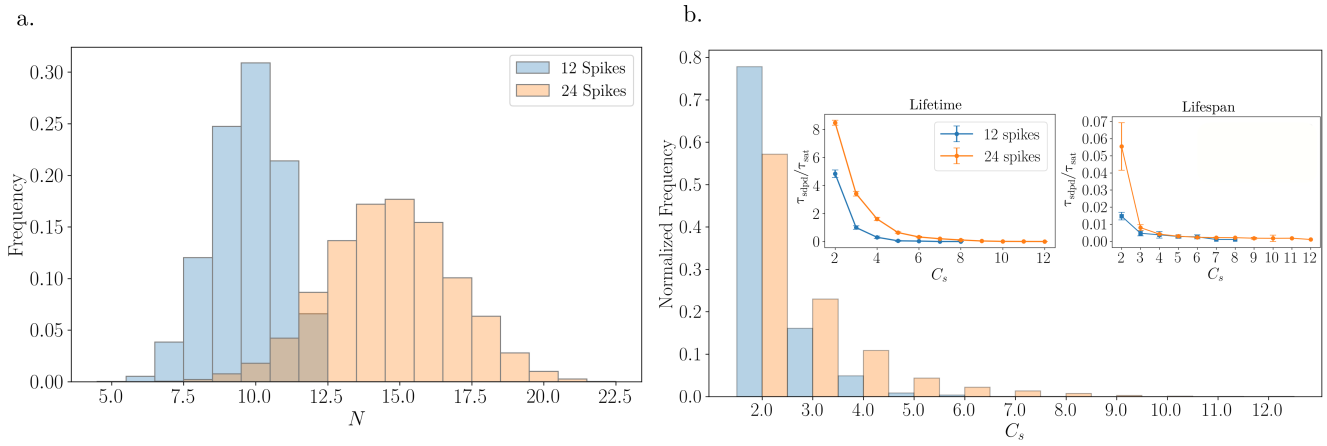

FIG. 6. a) Frequency of N number of clusters for the 12 and 24 spike proteins simulations. The histogram shows the most common values ranging from 9 to 10 N for the 12 spike proteins, while for the 24, the average number is around 15 N. b) Normalized frequency for the cluster size C_s for 12 and 24 spike protein simulations. Inside plots are the cluster lifetime $[\tau_{\text{sdpd}}/\tau_{sat}]$ for different C_s and the lifespan $[\tau_{\text{sdpd}}/\tau_{sat}]$ per C_s with error bars.

Our results show that incorporating structural flexibility into virus models leads to slight changes in rotational mobility compared to recently proposed rigid models. Interestingly, while flexibility does affect rotational motion, it does not significantly alter translational diffusion across the models we studied. Overall, we find that the viral envelope, due to its larger size, primarily determines the characteristic timescales of passive virion transport. Nonetheless, the dynamic behavior of spike proteins continues to impact viral mobility, despite their smaller size and faster timescales. This underscores the interplay between the motions of the envelope and the spikes in shaping the overall transport properties of the viruses.

Remarkably, the clustering behavior of spike proteins (particularly the frequent formation of transient triplets) mediated by hydrodynamic interactions poses the question about the potential functional role in viral infectivity. These simulation-based observations, which qualitatively align with reports from HIV studies,[9,51–53] point to a possible correlation between clustering properties, such as lifespan and aggregation probability, and the virus's ability to engage host cells. Although direct time-resolved experimental validation of real virions is currently limited, our results underscore the power of computational modeling to probe complex, time-dependent interactions that are difficult to capture in vitro. More broadly, the SDPD methodology introduced here provides a flexible framework for investigating nanoscale biological systems with similar structural and dynamical characteristics, extending beyond the specific case of virion transport.

ACKNOWLEDGMENTS

We acknowledge funding by the Basque Government through the BERC 2022-2025 program and by the Ministry of Science, Innovation and Universities: BCAM Severo Ochoa accreditation CEX2021-001142-S/MICIN/AEI/10.13039/501100011033. The Spanish State Research Agency through the project PID2020-117080RB-C55 funded by (AEI/FEDER, UE) with acronym COMPU-NANO-HYDRO. We thankfully acknowledge the computer resources at MareNostrum and the technical support provided by BSC (RES-FI-2024-3-0014 Mesoscale Modelling of Passive Transport of Viruses and Viral Spikes)

DATA AVAILABILITY STATEMENT

The data that support the findings of this study are available from the corresponding author upon reasonable request.

APPENDIX

Appendix A: Simulations Parameters and Relevant Time Scales

To characterize the spike proteins and the dynamics of the whole virion, we can identify different characteristic time scales, such as the sonic time, kinematic time, and Brownian time. The sonic time is given by $t_{cs} = R_s/c_s$, where R_s is the spike or envelope radius and c_s is the speed of sound. The kinematic time is $\tau_\nu = R_s^2/\nu$, where $\nu = \eta/\rho$ is the kinematic viscosity, and the Brownian time is $\tau_D = R_s^2/D$, with D the diffusion coefficient.

Taking into account that these time scales must satisfy the inequality $t_{cs} < \tau_\nu < \tau_D$[55], we set the thermal energy of the system as $k_B T = 1[\varepsilon_{\text{sdpd}}]$, the speed of sound $c_s = 40[l_{\text{sdpd}}/\tau_{\text{sdpd}}]$ and fluid viscosity $\eta = 5[m_{\text{sdpd}} l_{\text{sdpd}}/\tau_{\text{sdpd}}]$. The radius of each SDPD particle is $a = 0.1 l_{\text{sdpd}}$ the particle mass is $m = 0.008 m_{\text{sdpd}}$ and mass density $\rho_a = 1.9[m_{\text{sdpd}}/l_{\text{sdpd}}^2]$, yielding a thermal velocity $v_{th} = \sqrt{k_B T/m} = 11.2[l_{\text{sdpd}}/\tau_{\text{sdpd}}]$.

Similarly, for the envelope constructed with 3993 SDPD particles, the mass is $M = 3993m[m_{\text{sdpd}}]$, the mass density is $\rho_0 = M/V_e = 0.95[m_{\text{sdpd}}/l_{\text{sdpd}}^3]$, where $V_e = 4/3\pi R^3[l_{\text{sdpd}}^3]$ is the envelope volume. Finally, the thermal velocity of a envelope is $V_{th} = \sqrt{k_B T/M} = 0.177[l_{\text{sdpd}}/\tau_{\text{sdpd}}]$ Using these parameters, we compute the relevant time scales for the spike proteins with size $r_s = 0.24 l_{\text{sdpd}}$, we have $t_{cs} = 0.006 < \tau_\nu = 0.011 < \tau_D = 1.302$, whereas for the envelope with $R = 2l_{\text{sdpd}}$, we have $t_{cs} = 0.05 < \tau_\nu = 0.80 < \tau_D = 753.9$. In Table I , we give a breakdown of the key geometrical, physical, and simulation parameters used.

Additionally, we include other relevant dimensionless numbers that characterize the fluid regime in our simulations, such as Schmidt number $\text{Sc} = \nu/D$, Peclet number $\text{Pe} = V_{th} R_s/D$, and the Reynolds number $\text{Re} = \rho_0 V_{th}(2R_s)/\eta$ computed using the thermal velocity. To ensure numerical stability and lower density fluctuation, we use a time step size $dt = 0.001[\tau_{\text{sdpd}}]$, taking into account the criteria $dt < min(0.25h/c_s, 0.125h^2/\nu)$.[41]

Appendix B: Resolution Study

To ensure the accuracy of our simulations, we conduct a resolution study to determine the minimal spatial discretization required for reliable results. To determine the minimal resolution, we first estimate the spatial discretization that provides an adequate estimation of the rotational mobility ($M_0 = 1/(8\pi\eta R^3)$) of an spherical object in athermal conditions $k_B T = 0$. We focus on the rotational mobility as it is more sensitive to spatial discretization than translational mobility, due to its dependence on R^3. We simulate spherical envelopes for R/dx values in the range $\{5, 10, 15\}$, with

TABLE I. List of key parameters and dimensionless numbers. The length units are l_{sdpd}, time units are τ_{sdpd}, and mass units are m_{sdpd}.

Parameter	**Value**	**Units**
Geometrical		
Interparticle distance (dx)	0.2	l_{sdpd}
SDPD particle radius (a)	0.1	l_{sdpd}
Particle density (d)	$1/dx^3$	l_{sdpd}^{-3}
Radius of envelope (R/dx)	10	-
Radius of spike (r_s/dx)	2	-
Interaction radius (h/dx)	4	-
Physical Properties		
Density (ρ_0)	0.95	$m_{\text{sdpd}}/l_{\text{sdpd}}^3$
Mass particle (m)	0.008	m_{sdpd}
Mass envelope (M)	31.9	m_{sdpd}
Thermal energy ($K_b T$)	1	$\varepsilon_{\text{sdpd}}$
Viscosity (η)	5	$m_{\text{sdpd}}/(l_{\text{sdpd}}\tau_{\text{sdpd}})$
Speed of sound (c)	40	$l_{\text{sdpd}}/\tau_{\text{sdpd}}$
Thermal speed particle (v_{th})	11.2	$l_{\text{sdpd}}/\tau_{\text{sdpd}}$
Thermal speed envelope (V_{th})	0.17	$l_{\text{sdpd}}/\tau_{\text{sdpd}}$
Dimensionless Numbers		
Reynolds number (Re)	0.13	
Schmidt number (Sc)	988.7	
Peclet number (Pe)	133.4	
Time Parameters	**Envelope**	**Spike**
Time step (dt)	$1e^{-3}$	$1e^{-4}$
Diffusive time (τ_D)	753.9	1.302
Kinematic time (τ_ν)	0.8	0.011
Sonic time (τ_{cs})	0.05	0.006
Ratio τ_D/τ_ν	942.5	113.1

its center of mass fixed, and apply an external torque $\mathscr{T}$ along the z-axis, inducing a steady angular velocity ω_z in the xy-plane. To ensure consistency, the Reynolds number is kept as $\text{Re} \ll 1$ in all simulations. The numerical mobility is calculated as $M = \omega_z/\mathscr{T}$, and the ratio M/M_0 is used to identify the resolution that balances computational efficiency and accuracy. We identify that a ratio of $R/dx = 10$ provides a sufficient approximation of the rotational mobility, yielding a mobility ratio $M/M_0 \approx 1.05$.

After identifying this optimal resolution, we compute the rotational diffusion coefficient D_r^e and the translational diffusion coefficient D_t^e of an spherical envelope freely moving in a Newtonian fluid, using their mean square displacement (MSD) and mean square angular displacement (MSAD). We perform three independent realizations to ensure statistical robustness. The MSAD curve exhibits an early linear region before reaching a plateau, which is consistent with theoretical predictions, where this saturation occurs near $(\pi^2 - 4)/2$[48]. FIG. 7 presents the MSD and MSAD curves, averaged over the three realizations. We highlight the fitting intervals used for diffusion estimation, from 10 to $100\tau_\nu$ for rotational and translational diffusion. After applying the correction in the measured diffusion due to periodic boundary conditions, we estimate the relative errors of the diffusion coefficients with respect to the theoretical Stokes-Einstein relation, on the order of 6% and 24%, for D_t and D_r, respectively. Larger errors in rotational diffusion

are associated with its R^3 dependence, which amplifies the impact of finite-size effects.

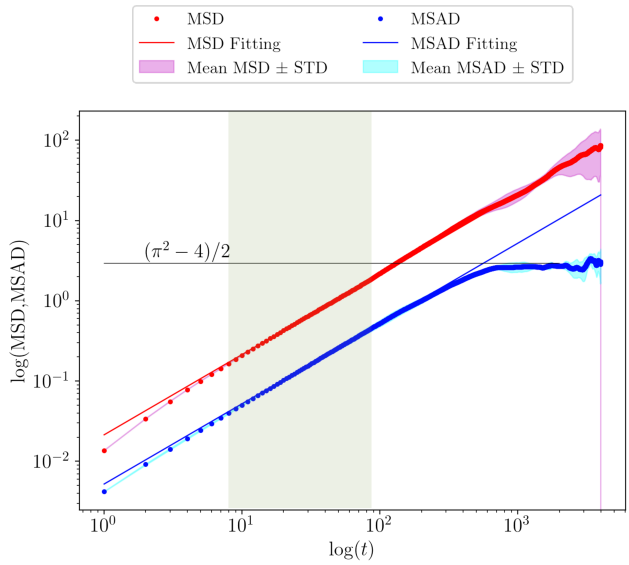

FIG. 7. Mean square displacement MSD and mean square angular displacement MSAD log-log curves for a spherical envelope under three different random fluid conditions. The shaded green region (10 to $100\tau_v$) marks the time interval used to estimate the rotational diffusion coefficient D_r^e and the translational diffusion coefficient D_t^e. The MSAD curve saturates near the theoretical limit $(\pi^2-4)/2$

Appendix C: Theoretical Tilt Angle Variation

TABLE II. Theoretical mean tilt angles β for different angular stiffness values K_α.

K_α	**Mean angle β (°)**	K_α	**Mean angle β (°)**
0	90.00	50	8.07
1	49.29	100	5.72
5	24.80	500	2.56
10	17.82	1000	1.81

Appendix D: Diffusion coefficients variations with K_α

TABLE III. Normalized diffusion coefficients ($\bar{D}_t$ and $\bar{D}_r$) with standard deviations for varying K_α values.

K_α	$\bar{D}_t \pm \sigma$	$\bar{D}_r \pm \sigma$
10	0.972 ± 0.002	0.947 ± 0.031
100	0.944 ± 0.059	0.924 ± 0.055
1000	1.018 ± 0.031	0.905 ± 0.045

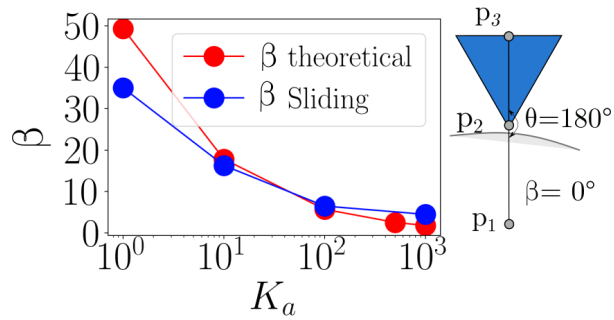

FIG. 8. Tilting angle β as a function of angular stiffness K_α (1 to 1000) for both theoretical predictions and simulation results on curved (envelope) surfaces. β is defined between three points: envelope center of mass (p_1), spike base (p_2), and spike tip (p_3). Higher K_α values restrict spike motion, reducing β.

Appendix E: Correction Factor for Diffusion Coefficients

To accurately compare simulated diffusion coefficients with theoretical predictions, correction factors are applied to account for finite-size effects in the simulation box.

1. Volume Fraction Calculation

The particle volume fraction ϕ is computed using the particle radius r and the cubic box length L:

$$\phi = \frac{4\pi R^3}{3L^3}$$

For this analysis, the parameters are:

$$R = 2, \quad L = 15$$

2. Translational Diffusion Correction Factor

The correction factor γ[46,55] for the translational diffusion coefficient D_t is calculated using an empirical formula:

$$a = 1.7601\phi^{1/3}, \quad b = 1.5593\phi^2,$$

$$c = 3.9799\phi^{8/3}, \quad d = 3.0734\phi^{10/3}$$

$$\gamma = 1 - a + \phi - b + c - d$$

The corrected translational diffusion coefficient is given by:

$$D_t = D_t^o \gamma = \frac{\gamma}{6\pi\eta R}$$

where D_t^o is the classical Stokes-Einstein coefficient, $\eta = 5$ is the fluid viscosity, and R is the hydrodynamic (envelope) radius.

3. Rotational Diffusion Correction Factor

A correction factor C is applied to the rotational diffusion coefficient[56]. The corrected rotational diffusion is given by:

$$C = \frac{1}{6\eta L^3}$$

$$D_r = D_r^o - C = \left(\frac{1}{8\pi\eta R^3}\right) - C$$

where D_r^o is the classical Stokes-Einstein expression for rotational diffusion.

In this case, the correction factor C is less significant than for the translational case.

4. Comparison Between Simulated and Corrected Diffusion

The simulated diffusion coefficients D_t^{simul} and D_r^{simul} are normalized by their respective corrected values:

$$\frac{D_t^{\text{simul}}}{D_t}, \quad \frac{D_r^{\text{simul}}}{D_r}$$

These ratios provide insight into how closely the simulation results match theoretical expectations, accounting for both system size and viscosity.

Appendix F: Mean Squared Angular Displacement (MSAD)

The Mean Squared Angular Displacement (MSAD) quantifies the rotational diffusion of particles using spherical coordinates derived from 3D Cartesian data.

To compute angular displacement, Cartesian coordinates (x, y, z) are first converted to spherical coordinates (r, θ, ϕ) using the following formulas:

$$r = \sqrt{x^2 + y^2 + z^2}$$

$$\theta = \cos^{-1}\left(\frac{z}{r}\right) \quad \text{if } r \neq 0$$

$$\phi = \tan^{-1}(y, x)$$

If $r = 0$, both θ and ϕ are set to 0.

The MSAD is computed for each lag time Δt as follows:

$$\Delta\alpha^2 = \left[\cos^{-1}\left(\sin(\phi_1)\sin(\phi_2) + \cos(\phi_1)\cos(\phi_2)\cos(\theta_1 - \theta_2)\right)\right]^2$$

.

Where $\phi_1 = \phi(t + \Delta t)$, $\phi_2 = \phi(t)$, $\phi_1 = \theta_1(t + \Delta t)$ and $\theta_2 = \phi(t)$

$$\text{MSAD}(\Delta t) = \frac{1}{N - \Delta t} \sum_{t=1}^{N-\Delta t} \Delta\alpha^2(\Delta t)$$

Diffusion coefficient estimation: From MSAD curve, the rotational diffusion coefficient D_r is computed using the following equation:

$$\text{MSAD}(\Delta t) = 4D_r t \Rightarrow \quad D_r = \frac{\text{MSAD}(t)}{4t}$$

Appendix G: Mean Squared Displacement (MSD)

The Mean Squared Displacement (MSD) is a widely used metric for characterizing translational diffusion from particle trajectory data in 3D space.

For each lag time Δt, the displacement is computed in each spatial dimension:

$$\Delta x_i(\Delta t) = x(t_i + \Delta t) - x(t_i)$$

$$\Delta y_i(\Delta t) = y(t_i + \Delta t) - y(t_i)$$

$$\Delta z_i(\Delta t) = z(t_i + \Delta t) - z(t_i)$$

The total squared displacement is:

$$\Delta r_i^2(\Delta t) = (\Delta x_i)^2 + (\Delta y_i)^2 + (\Delta z_i)^2$$

The MSD is obtained by averaging over all valid starting points:

$$\text{MSD}(\Delta t) = \frac{1}{N - \Delta t} \sum_{i=1}^{N-\Delta t} \Delta r_i^2(\Delta t)$$

MSD can be decomposed into its directional components:

$$\text{MSD}_x(\Delta t) = \frac{1}{N - \Delta t} \sum_{i=1}^{N-\Delta t} (\Delta x_i)^2$$

$$\text{MSD}_y(\Delta t) = \frac{1}{N - \Delta t} \sum_{i=1}^{N-\Delta t} (\Delta y_i)^2$$

$$\text{MSD}_z(\Delta t) = \frac{1}{N - \Delta t} \sum_{i=1}^{N-\Delta t} (\Delta z_i)^2$$

Diffusion Coefficient Estimation: From the MSD curve, the translational diffusion coefficient D_t is extracted using theoretical formulations:

$$\text{MSD}(t) = 6D_t t \quad \Rightarrow \quad D_t = \frac{\text{MSD}(t)}{6t}$$

Appendix H: Geodesic Mean Squared Displacement (gMSD)

The geodesic MSD (gMSD)[47,48] accounts for angular distances on a spherical surface and is useful for confined diffusion on curved surfaces.

The gMSD is computed using the spherical law of cosines multiplied by the envelope radius R:

$$\mathrm{gMSD}(\Delta t) = \frac{1}{N-\Delta t}\sum_{i=1}^{N-\Delta t}\Delta d^2(\Delta t)$$

$$\Delta d^2 = \left[R\cos^{-1}\left(\sin(\phi_1)\sin(\phi_2)+\cos(\phi_1)\cos(\phi_2)\cos(\theta_1-\theta_2)\right)\right]^2$$

However, we convert them to Cartesian coordinates on the unit sphere using unit vectors to compute the angular displacement,

$$\vec{u}(\theta,\phi) = \begin{bmatrix} x \\ y \\ z \end{bmatrix} = \begin{bmatrix} \sin(\theta)\cos(\phi) \\ \sin(\theta)\sin(\phi) \\ \cos(\theta) \end{bmatrix}.$$

These vectors describe the direction of each point.

We compute the angular displacement by computing angle α_i between $\vec{u}_i$ and $\vec{u}_{i+\Delta t}$ that corresponds to time steps i and $i+\Delta t$. To compute α, we calculate the dot product of the unit vectors, $\alpha_i = \cos^{-1}(\vec{u}_i \cdot \vec{u}_{i+\Delta t})$ where $\vec{u}_i \cdot \vec{u}_{i+\Delta t} = \cos(\alpha_i)$.

Once the value of α is computed we can determine the angular displacement, $d = R \cdot \alpha_i$, where R is the envelope radius. The squared displacement is Δd^2, that is the one we compute in the *gMSD* formula.

Diffusion Coefficient Estimation: From the gMSD curve, the translational diffusion coefficient D_t is extracted using theoretical formulations:

$$\mathrm{gMSD}(t) = 4D_t t \quad \Rightarrow \quad D_t = \frac{\mathrm{gMSD}(t)}{4t}$$

Appendix I: Translational Diffusion of Spike Proteins Over the Envelope

We compute the D_{sp} within the range 1–10, τ_v. Across all spike counts, the gMSD curves exhibit similar behavior, initially linear $\alpha = 1$, before transitioning to a plateau, indicating a saturation regime. The values of D_{sp} remain relatively consistent across all three configurations, as expected in confined diffusion. Given the diffusion coefficient D_{sp}, we define the saturation time as: $\tau_{\mathrm{sat}} = R^2/D_{sp} = 90\tau_{\mathrm{sdpd}}$.

As a theoretical case, we can compute the Stokes-Einstein translational diffusion over a surface,

$$D_t = \frac{k_B T}{4\pi\eta r_s} = 0.039.$$

TABLE IV. Spike translational diffusion coefficients.

Number of spikes proteins	$D_{sp}[l^2_{\mathrm{sdpd}}/\tau_{\mathrm{sdpd}}]$	$\tau_{sat}[\tau_{\mathrm{sdpd}}]$
Stokes-Einstein 2D	0.039	100
2	$0.044 \pm 2\times10^{-3}$	90.5
12	$0.045 \pm 2\times10^{-4}$	89.3
24	$0.045 \pm 3\times10^{-5}$	89.5

REFERENCES

[1] A. Valero-Rello, C. Baeza-Delgado, I. Andreu-Moreno, and R. Sanjuán, "Cellular receptors for mammalian viruses," PLoS Pathogens **20**, e1012021 (2024).

[2] B. Turoňová, M. Sikora, C. Schürmann, W. J. Hagen, S. Welsch, F. E. Blanc, S. von Bülow, M. Gecht, K. Bagola, C. Hörner, *et al.*, "In situ structural analysis of sars-cov-2 spike reveals flexibility mediated by three hinges," Science **370**, 203–208 (2020).

[3] D. Chmielewski, E. A. Wilson, G. Pintilie, P. Zhao, M. Chen, M. F. Schmid, G. Simmons, L. Wells, J. Jin, A. Singharoy, *et al.*, "Structural insights into the modulation of coronavirus spike tilting and infectivity by hinge glycans," Nature communications **14**, 7175 (2023).

[4] T. Sakai, H. Takagi, Y. Muraki, and M. Saito, "Unique Directional Motility of Influenza C Virus Controlled by Its Filamentous Morphology and Short-Range Motions," Journal of virology (2018), 10.1128/JVI.01522-17.

[5] M. D. Vahey and D. A. Fletcher, "Influenza A virus surface proteins are organized to help penetrate host mucus," eLife **8** (2019), 10.7554/eLife.43764.

[6] L. Stevens, S. De Buyl, and B. M. Mognetti, "The sliding motility of the bacilliform virions of Influenza A viruses," Soft Matter **19**, 4491 (2023).

[7] S. Yang, G. Hiotis, Y. Wang, J. Chen, J.-h. Wang, M. Kim, E. L. Reinherz, and T. Walz, "Dynamic hiv-1 spike motion creates vulnerability for its membrane-bound tripod to antibody attack," Nature Communications **13**, 6393 (2022).

[8] L. Andronov, M. Han, Y. Zhu, A. Balaji, A. R. Roy, A. E. Barentine, P. Patel, J. Garhyan, L. S. Qi, and W. E. Moerner, "Nanoscale cellular organization of viral rna and proteins in sars-cov-2 replication organelles," Nature Communications **15** (2024), 10.1038/s41467-024-48991-x.

[9] I. Carlon-Andres, T. Malinauskas, and S. Padilla-Parra, "Structure and Dynamics of HIV-1 Env Trimers on Native Virions Engaged in Living T Cells," SSRN Electronic Journal (2020), 10.2139/ssrn.3589838.

[10] H. R. Gelderblom, M. 0zel, and G. Pauli, "Morphogenesis and morphology of HIV Structure-function relations Brief Review," Tech. Rep. (1989).

[11] J. Chojnacki, D. Waithe, P. Carravilla, N. Huarte, S. Galiani, J. Enderlein, and C. Eggeling, "Envelope glycoprotein mobility on HIV-1 particles depends on the virus maturation state," Nature Communications **8** (2017), 10.1038/s41467-017-00515-6.

[12] Y. G. Kuznetsov and A. McPherson, "Atomic force microscopy in imaging of viruses and virus-infected cells," Microbiology and Molecular Biology Reviews **75**, 268–285 (2011), https://journals.asm.org/doi/pdf/10.1128/mmbr.00041-10.

[13] T. Ando, T. Uchihashi, and T. Fukuma, "High-speed atomic force microscopy for nano-visualization of dynamic biomolecular processes," Progress in Surface Science **83**, 337–437 (2008).

[14] W. Godinez, M. Lampe, S. Wörz, B. Müller, R. Eils, and K. Rohr, "Deterministic and probabilistic approaches for tracking virus particles in time-lapse fluorescence microscopy image sequences," Medical Image Analysis **13**, 325–342 (2009), includes Special Section on Functional Imaging and Modelling of the Heart.

[15] R. Gordon, "[invited] biosensing with nanoaperture optical tweezers," Optics and Laser Technology **109**, 328–335 (2019).

[16] C. J. Bustamante, Y. R. Chemla, S. Liu, and M. D. Wang, "Optical tweezers in single-molecule biophysics," Nature Reviews Methods Primers **1**, 25 (2021).

[17] G. Katz, Y. Benkarroum, H. Wei, W. J. Rice, D. Bucher, A. Alimova, A. Katz, J. Klukowska, G. T. Herman, and P. Gottlieb, "Morphology of influenza b/lee/40 determined by cryo-electron microscopy," PLOS ONE **9**, 1–8 (2014).

[18]Z. Ke, J. Oton, K. Qu, M. Cortese, V. Zila, L. McKeane, T. Nakane, J. Zivanov, C. J. Neufeldt, B. Cerikan, J. M. Lu, J. Peukes, X. Xiong, H. G. Kräusslich, S. H. Scheres, R. Bartenschlager, and J. A. Briggs, "Structures and distributions of SARS-CoV-2 spike proteins on intact virions," Nature **588**, 498–502 (2020).

[19]A. Slater, N. Nair, R. Suétt, R. Mac Donnchadha, C. Bamford, S. Jasim, D. Livingstone, and E. Hutchinson, "Visualising viruses," Journal of General Virology **103**, 001730 (2022), https://doi.org/10.1099/jgv.0.001730.

[20]E. E. Jefferys and M. S. P. Sansom, "Chapter 10: Computational virology: Molecular simulations of virus dynamics and interactions," in *Physical Virology*, Advances in Experimental Medicine and Biology, Vol. 1215, edited by U. F. Greber (Springer Nature Switzerland AG, Cham, 2019).

[21]S. Borkotoky, D. Dey, Z. Hazarika, A. Joshi, and K. Tripathi, "Unravelling viral dynamics through molecular dynamics simulations - a brief overview," Biophysical Chemistry **291**, 106908 (2022).

[22]H. Ode, M. Nakashima, S. Kitamura, W. Sugiura, and H. Sato, "Molecular dynamics simulation in virus research," Frontiers in microbiology **3**, 258 (2012).

[23]M. R. Machado and S. Pantano, "Fighting viruses with computers, right now," Current Opinion in Virology **48**, 91–99 (2021).

[24]P. E. Jones, C. Pérez-Segura, A. J. Bryer, J. R. Perilla, and J. A. Hadden-Perilla, "Molecular dynamics of the viral life cycle: progress and prospects," Current Opinion in Virology **50**, 128–138 (2021).

[25]D. L. Lynch, A. Pavlova, Z. Fan, and J. C. Gumbart, "Understanding virus structure and dynamics through molecular simulations," Journal of chemical theory and computation **19**, 3025–3036 (2023).

[26]Y. Li, Y. L. Zhu, Y. C. Li, H. J. Qian, and C. C. Sun, "Self-assembly of two-patch particles in solution: a Brownian dynamics simulation study," http://dx.doi.org/10.1080/08927022.2013.819430 **40**, 449–457 (2014).

[27]M. A. Islam, S. Barua, and D. Barua, "A multiscale modeling study of particle size effects on the tissue penetration efficacy of drug-delivery nanoparticles," BMC Systems Biology **11** (2017), 10.1186/S12918-017-0491-4.

[28]J. Ilnytskyi, "Self-Assembly of Nanoparticles Decorated by Liquid Crystalline Groups: Computer Simulations," Self-Assembly of Nanostructures and Patchy Nanoparticles (2020), 10.5772/INTECHOPEN.89682.

[29]V. E. Debets, L. M. C. Janssen, and A. S. Saric, "Characterising the diffusion of biological nanoparticles on fluid and cross-linked membranes," Soft Matter **16**, 10628 (2020).

[30]J. Liu, R. Tourdot, V. Ramanan, N. J. Agrawal, and R. Radhakrishanan, "Mesoscale simulations of curvature-inducing protein partitioning on lipid bilayer membranes in the presence of mean curvature fields," (2012).

[31]N. Moreno, B. Sutisna, and E. Fried, "Entropic factors and structural motifs of triblock-terpolymer-based patchy nanoparticles," Royal Society of Chemistry (2020), 10.1039/D0NR06192A.

[32]S. B. Chen, "Dissipative Particle Dynamics Simulation of Nanoparticle Diffusion in a Crosslinked Polymer Network," The Journal of Physical Chemistry B (2022), 10.1021/ACS.JPCB.2C05217.

[33]L. Li, X. Li, Z. Duan, R. J. Meyer, R. Carr, S. Raman, L. Koziol, and G. Henkelman, "Adaptive kinetic Monte Carlo simulations of surface segregation in PdAu nanoparticles," Nanoscale **11**, 10524–10535 (2019).

[34]M. A. Kanso, J. H. Piette, J. A. Hanna, and A. J. Giacomin, "Coronavirus rotational diffusivity," Physics of Fluids **32** (2020), 10.1063/5.0031875.

[35]M. A. Kanso, V. Chaurasia, E. Fried, and A. J. Giacomin, "Peplomer bulb shape and coronavirus rotational diffusivity," Physics of Fluids **33** (2021), 10.1063/5.0048626.

[36]F. Balboa Usabiaga and B. Delmotte, "A numerical method for suspensions of articulated bodies in viscous flows," Journal of Computational Physics **464**, 111365 (2022).

[37]N. Moreno, D. M. Chaparro, and F. B. Usabiaga, "Hydrodynamics of spike proteins dictate a transport - affinity competition for SARS - CoV - 2 and other enveloped viruses," Scientific Reports , 1–13 (2022).

[38]D. Moreno-Chaparro, N. Moreno, F. B. Usabiaga, and M. Ellero, "Computational modeling of passive transport of functionalized nanoparticles," The Journal of Chemical Physics **158**, 104108 (2023), https://pubs.aip.org/aip/jcp/article-pdf/doi/10.1063/5.0136833/16791431/104108_1_online.pdf.

[39]P. Espanol and M. Revenga, "Smoothed dissipative particle dynamics," Phys. Rev. E **67**, 026705 (2003).

[40]M. Ellero and P. Espanol, "Everything you always wanted to know about SDPD (but were afraid to ask)," Appl. Math. Mech.-Engl. Ed **39**, 103–124 (2018).

[41]J. J. Monaghan, "Smoothed particle hydrodynamics," In: Annual review of astronomy and astrophysics. Vol. 30 (A93-25826 09-90), p. 543-574. **30**, 543–574 (1992).

[42]N. Moreno and M. Ellero, "Arbitrary flow boundary conditions in smoothed dissipative particle dynamics: A generalized virtual rheometer," Physics of Fluids **33**, 012006 (2021), https://pubs.aip.org/aip/pof/article-pdf/doi/10.1063/5.0035936/15853287/012006_1_online.pdf.

[43]E. Zohravi, N. Moreno, and M. Ellero, "Computational mesoscale framework for biological clustering and fractal aggregation," Soft Matter **19**, 7399–7411 (2023).

[44]E. Zohravi, N. Moreno, K. Hawkins, D. Curtis, and M. Ellero, "Mesoscale modelling of fibrin clots: the interplay between rheology and microstructure at the gel point," Soft Matter **21**, 1141–1151 (2025).

[45]S. Espinosa-Moreno, N. Moreno, and M. Ellero, "Computational modelling of thixotropic multiphase fluids using smoothed dissipative particle dynamics," Arxiv (2025).

[46]A. Vázquez-Quesada and M. Ellero, "GENERIC-compliant simulations of Brownian multi-particle systems: modeling stochastic lubrication," SeMA Journal **79**, 165–185 (2022).

[47]A. Ledesma-Durán, J. Munguía-Valadez, J. A. Moreno-Razo, S. I. Hernández, and I. Santamaría-Holek, "Entropic Effects of Interacting Particles Diffusing on Spherical Surfaces," Frontiers in Physics **9** (2021), 10.3389/fphy.2021.634792.

[48]A. Ledesma-Durán and L. H. Juárez-Valencia, "Diffusion coefficients and MSD measurements on curved membranes and porous media," (2023).

[49]X. Bian, S. Litvinov, R. Qian, M. Ellero, and N. Adams, "Multiscale modeling of particle in suspension with smoothed dissipative particle dynamics," Physics of Fluids **24** (2012), 10.1063/1.3676244.

[50]A. Einstein, "On the movement of small particles suspended in stationary liquids required by the molecular," Ann. d. Phys (1905).

[51]D. J. Williamson, C. Zaza, I. Carlon-Andres, T. Starling, A. Gentili, J. W. Thrush, A. Le Bas, R. T. Ravi, S. Neil, R. J. Owens, M. Dumoux, S. Simoncelli, and S. Padilla-Parra, "Single-molecule localisation microscopy approaches reveal envelope glycoprotein clusters in single-enveloped viruses: a potential functional role?" Biochemical Society Transactions , BST20240769 (2025).

[52]J. Liu, A. Bartesaghi, M. J. Borgnia, G. Sapiro, and S. Subramaniam, "Molecular architecture of native HIV-1 gp120 trimers," Nature **455**, 109–113 (2008).

[53]B. K. Ganser-Pornillos, M. Yeager, and O. Pornillos, "Assembly and architecture of HIV," Advances in Experimental Medicine and Biology **726**, 441–465 (2012).

[54]A. Harris, G. Cardone, D. C. Winkler, J. B. Heymann, M. Brecher, J. M. White, and A. C. Steven, "Influenza virus pleiomorphy characterized by cryoelectron tomography," Proceedings of the National Academy of Sciences of the United States of America **103**, 19123–19127 (2006).

[55]J. Padding and A. Louis, "Hydrodynamic interactions and brownian forces in colloidal suspensions: Coarse-graining over time and length scales," Physical Review E—Statistical, Nonlinear, and Soft Matter Physics **74**, 031402 (2006).

[56]M. Linke, J. Köfinger, and G. Hummer, "Rotational diffusion depends on box size in molecular dynamics simulations," The journal of physical chemistry letters **9**, 2874–2878 (2018).